RESEARCH ARTICLE

Energy Conversion and Storage

Energy & Environmental Materials WILEY

Polycarbazole–NiOOH Interfacial Engineering of $BiVO_4$ Photoanodes for Efficient and Stable Solar Water Splitting

Lakshman Sundar Arumugam, Ana Gutierrez-Blanco, Agustin O. Alvarez, Alejandro Saura Aviles, Mahesh Eledath-Changarath, Rafael Abargues, Juan Francisco Sánchez-Royo, Helena Rabelo, Maria Chiara Spadaro, Jordi Arbiol, Javier E. Durantini, and Sixto Giménez**

Photoelectrochemical (PEC) water splitting is a promising strategy for sustainable hydrogen and chemical production. Among candidate photoanodes, bismuth vanadate (BVO) offers a suitable band gap (∼2.4 eV) and favorable band-edge alignment for water oxidation, yet its performance remains limited by inefficient charge separation, severe surface recombination, and sluggish interfacial kinetics. Here, these challenges are addressed through the electro-polymerization of a π-conjugated carbazole (p-CBZ) layer on BVO, forming a p–n heterojunction that enhances the built-in electric field, accelerates hole transport, and passivates surface defects. The subsequent deposition of NiOOH as an oxygen evolution co-catalyst further promotes charge transfer and catalytic activity. The resulting BVO/p-CBZ/NiOOH hybrid photoanode achieves a photocurrent density of 5.6 mA cm^{-2} at 1.23 V versus RHE under 1 sun illumination and maintains stable water oxidation for over 72 h. Further mechanistic insights using electrochemical impedance (EIS) and light-modulated spectroscopies (IMPS/IMVS) confirm that p-CBZ markedly improves charge separation and carrier diffusion, while NiOOH facilitates oxygen evolution. This synergistic design significantly enhances PEC performance, highlighting π-conjugated carbazole polymers as effective hole extraction and passivation layers in BVO-based photoanodes for efficient and durable solar-driven water splitting.

1. Introduction

The pursuit of sustainable energy solutions has driven extensive research into water oxidation, a key reaction for renewable hydrogen production within artificial photosynthesis systems.[1] Among the many semiconductors investigated for photoelectrochemical (PEC) water oxidation, including WO_3,[2] Si,[3] TiO_2,[4] CN,[5] and α-Fe_2O_3,[6] $BiVO_4$ (BVO) has emerged as a particularly promising candidate. This is attributed to its advantageous features, such as the relative abundance of its constituent elements,[7] favorable energy band alignment for water oxidation[8] and low processing cost.[9] Nevertheless, BVO suffers from intrinsic drawbacks, including sluggish water oxidation kinetics,[10] rapid recombination of photogenerated electron–hole pairs,[7] poor charge carrier mobility, and short carrier diffusion lengths (≈70 nm).[11]

To address these limitations, considerable efforts have focused on exploiting the distinctive electronic structure and surface chemistry of BVO through diverse modification strategies. These include metal-ion doping,[12] surface passivation,[13] heterojunction formation,[14] nanostructuring,[15] plasmonic enhancement,[16] photo charging,[7,9,17] and surface modifications.[18,19] Another highly effective approach involves loading oxygen evolution co-catalysts onto BVO,[20] which improves surface catalytic activity,[21] suppresses surface recombination,[22] and enhances both stability[23] and durability.[24] In parallel, the integration of functional charge-transport layers between BVO and co-catalysts has been shown to facilitate charge separation and transport, minimize recombination losses, and optimize band alignment.[25–27]

In this context, the deposition of organic materials onto semiconducting photoanodes has emerged as a promising strategy for the design of hybrid materials with tailored optoelectronic and catalytic properties.[28] Synergistic interactions between organic and inorganic components can enhance light absorption,[29–31] strengthen the interfacial electric field,[32] improve charge mobility and separation,[33,34] increase catalytic efficiency,[35,36] and prolong long-term operational stability.[32,37] Various organic molecules, including graphene oxide,[38] graphitic carbon nitride,[39] poly (3-hexylthiophene),[40]

L. S. Arumugam, Dr. A. Gutierrez-Blanco, Dr. J. E. Durantini, Prof. S. Giménez
Institute of Advanced Materials, Universitat Jaume I, Avinguda de Vicent Sos Baynat, s/n, 12006, Castelló de la Plana, Spain
E-mail: durantin@uji.es
E-mail: sjulia@uji.es
Dr. A. O. Alvarez
AMOLF, Science Park 104, 1098 XG, Amsterdam, The Netherlands
A. Saura Aviles, M. Eledath-Changarath, Dr. R. Abargues, Prof. J. F. Sánchez-Royo
Instituto de Ciencia de los Materiales de la Universidad de Valencia (ICMUV), Paterna 46980, València, Spain
H. Rabelo, Dr. M. C. Spadaro, Prof. J. Arbiol
Catalan Institute of Nanoscience and Nanotechnology (ICN2), CSIC and BIST, Campus UAB, Bellaterra, 08193, Barcelona, Spain
Dr. M. C. Spadaro
Department of Physics and Astronomy "Ettore Majorana" and IMM-CNR, University of Catania, S. Sofia 64, Catania 95123, Italy
Prof. J. Arbiol
ICREA, Pg. Lluís Companys 23, 08010, Barcelona, Catalonia, Spain
The ORCID identification number(s) for the author(s) of this article can be found under https://doi.org/10.1002/eem2.70354.

DOI: 10.1002/eem2.70354

polycarbazole,[41] covalent organic frameworks,[29] etc., have been explored as charge-transport layers or structural modifiers to boost PEC performance.

In particular, coupling a hole transport layer (HTL) with a BVO photoanode via p–n heterojunction formation enables favorable band bending and efficient interfacial hole transfer at the semiconductor/electrolyte interface (SEI).[25,37] For optimal function, HTLs must exhibit suitable band alignment with BVO to ensure that photogenerated holes can overcome the 1.23 V versus RHE thermodynamic threshold for water oxidation, while also providing sufficient conductivity for efficient charge transport.[42,43] Among available HTLs, polycarbazoles are especially attractive owing to their excellent hole conductivity, wide bandgap, tunable electronic structure, and favorable film-forming characteristics.[41,44] Beyond PEC applications, carbazole-based polymers have been widely employed in organic and perovskite solar cells,[45,46] energy storage devices,[47] and electrochemical sensors,[48] underscoring their versatility and efficiency in energy conversion technologies.[44,49]

Therefore, the integration of carbazole with BVO presents an opportunity to combine the complementary advantages of both components, yielding hybrid materials with enhanced charge-transport and catalytic properties.[41] For instance, Xu and co-workers reported a hybrid p-CBZ/Sb_2S_3 photoanode delivering a photocurrent density of 10.1 mA cm^{-2} at 1.23 V versus RHE with stable operation exceeding 100 h,[50] while Jang and co-workers demonstrated a $NiFeCoO_x$/p-CBZ/Mo:$BiVO_4$ system achieving 6.66 mA cm^{-2} at 1.23 V *vs* RHE, with stability maintained over 5 h.[41] In both cases, electro-polymerized carbazole served as an effective HTL. However, when directly applied to BVO, a decline in stability has been observed, consistent with reports that functional interlayers often enhance either photocurrent density or long-term stability, but rarely both simultaneously. Overcoming this trade-off to achieve simultaneous improvements in photocurrent output and durability, along with elucidating the underlying mechanisms, remains a critical challenge in PEC photoanode design.[32,43,51]

In this study, we introduce a multilayer heterojunction photoanode comprising BVO, an electro-polymerized carbazole interlayer (p-CBZ), and a NiOOH co-catalyst, designed to overcome key limitations of conventional BVO architectures. The p-CBZ layer, deposited with finely controlled thickness, functions as a passivating and conductive interface that suppresses surface recombination, while facilitating efficient hole transfer. Complementarily, the NiOOH overlayer accelerates water oxidation kinetics by providing a highly active, hydroxyl-rich catalytic surface. Working in concert, these engineered layers enhance charge separation, strengthen band bending, and markedly increase catalytic activity, yielding photocurrent densities of ≈5.6 mA cm^{-2} at 1.23 V versus RHE together with operational stability exceeding ≈70 h, surpassing the stability over previously reported organic-based interlayers. Using a comprehensive suite of in situ and ex situ techniques, including X-ray photoelectron spectroscopy (XPS), electrochemical impedance spectroscopy (EIS), optoelectronic analyses, and photoelectrochemical characterization, we unravel how the multilayer architecture modulates interfacial electronic structure and carrier dynamics, providing insights beyond prior polycarbazole-based heterostructures. Overall, our findings establish a general strategy for simultaneously improving both efficiency and durability in BVO-based photoanodes. This multilayer design thus represents a promising avenue for the development of high-performance PEC water-splitting systems.

2. Results and Discussion

2.1. Fabrication and Characterization of BVO and Modified BVO Photoanodes

Figure 1a shows the fabrication of BVO films on FTO substrates, followed by electro-polymerization of the carbazole (CBZ) hole transport layer (Figure 1b). Various electro-polymerization conditions were tested to optimize the performance of the BVO/p-CBZ photoanodes (Figure S1a, Supporting Information). During CBZ oxidation, well-established radical cation coupling reactions[52] lead to polymer growth, which was confirmed by repeated cyclic voltammetry (CV) scans (Figure S2, Supporting Information). The progressive increase in oxidation and reduction currents indicated the formation of an electroactive film, consistent with the accumulation of polymerized species.[53] A corresponding rise in capacitive current with additional CV cycles reflected thickening of the p-CBZ layer,[50] which adversely affected photocurrent density (Figure S1b, Supporting Information). This decline is attributed to the longer transport path for photogenerated holes as observed in most of the polymer/photoanode architectures. This decreases the effective charge separation as the carrier diffusion lengths in polymers are shortened with thicker layers, further promoting charge recombination.[54] Optimal PEC performance was obtained after two CV cycles of CBZ deposition. To further accelerate oxygen evolution kinetics, nickel oxyhydroxide (NiOOH) was employed as the oxygen evolution catalyst (OEC) and electrodeposited from a $NiCl_2 \cdot 6H_2O$ solution, as outlined in Figure 1b. Detailed experimental procedures are provided in the Experimental section.

The morphology and structure of the synthesized photoanodes were examined by scanning electron microscopy (SEM), bright field transmission electron microscopy (BF TEM), and high angle annular dark field scanning transmission electron microscopy (HAADF TEM). Top-view SEM images of the pristine BVO films (Figure 1c and Figure S3, Supporting Information) reveal a nanostructured, worm-like porous morphology, consistent with earlier reports.[33,51] After p-CBZ electro-polymerization, the overall surface morphology remains largely unchanged (Figure 1d and Figure S4, Supporting Information), indicating that the polymer layer does not disrupt the underlying BVO architecture. By contrast, the BVO/p-CBZ/NiOOH photoanode (Figure 1e and Figure S4, Supporting Information) displays a roughened surface, a feature known to promote enhanced PEC activity.[43] BF TEM analysis of BVO (Figure 1f) shows hexagonal nanoparticles of ≈35 nm with an interplanar spacing of ≈3.1 Å, corresponding to the (121) plane of monoclinic BVO.[41,55] Following NiOOH deposition, a conformal overlayer is observed on the BVO surface (Figure S4, Supporting Information). HR-TEM and HAADF STEM images of BVO/p-CBZ (Figure 1g,i–j and Figure S5a, Supporting Information) further confirm the presence of a uniform p-CBZ layer with a thickness of ≈10 nm. For the BVO/p-CBZ/NiOOH photoanode, HR-TEM and HAADF STEM images (Figure 1h,k–l and Figure S5b, Supporting Information) clearly show sequential stacking of the BVO, p-CBZ, and NiOOH layers. Elemental mapping by EDS (Figure 1m) verifies the homogeneous distribution of Bi, V, C, O, and Ni, confirming successful deposition of both p-CBZ and NiOOH.[25]

The crystalline structure and phase purity of the photoanodes were examined by X-ray diffraction (XRD) (Figure S6, Supporting Information). The diffraction peaks correspond well to the monoclinic phase of

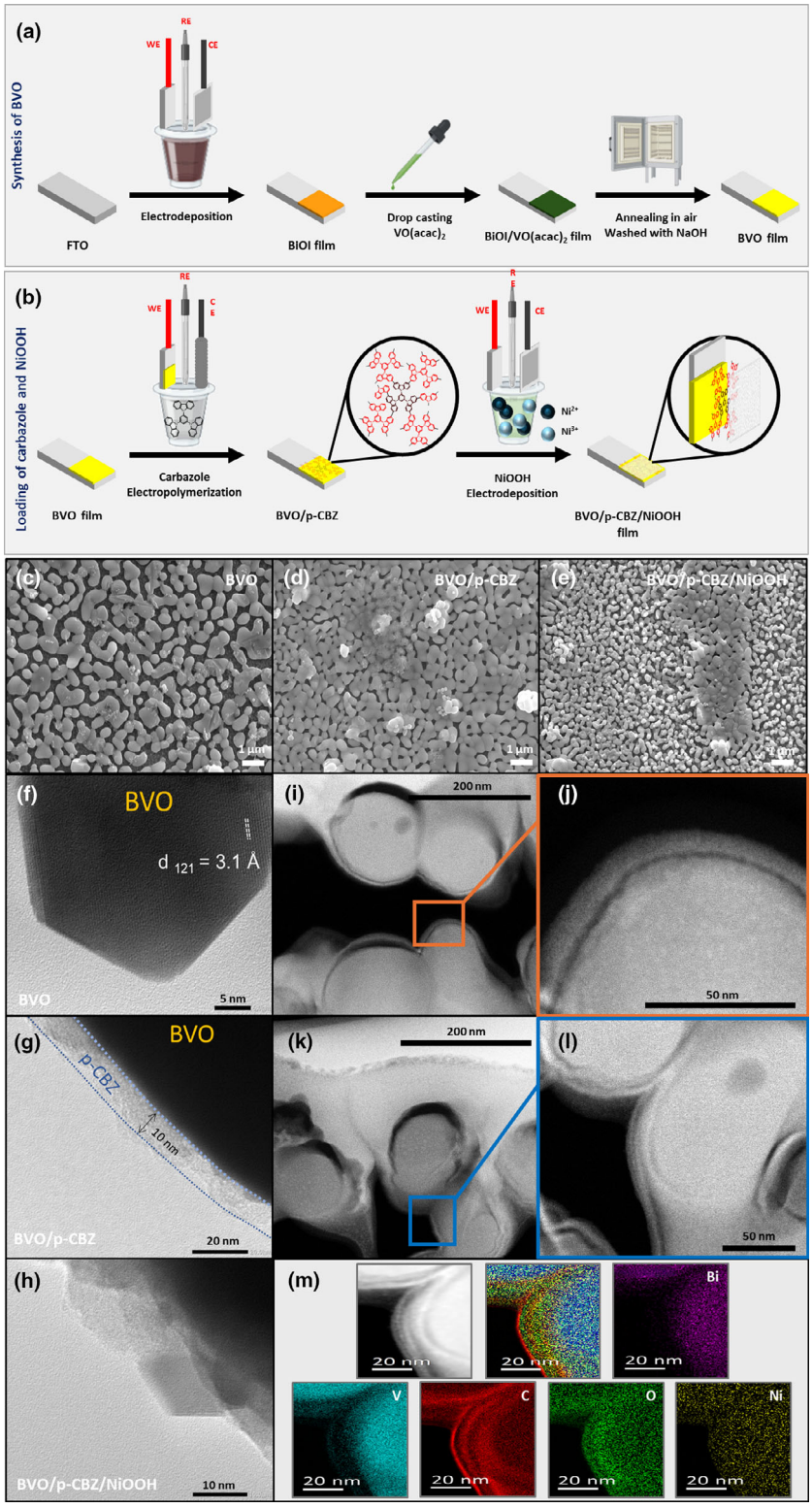

Figure 1. Schematic synthetic route of a) BVO photoanodes and b) electrodeposition of p-CBZ and NiOOH onto BVO photoanodes. Top-view SEM images of c) BVO, d) BVO/p-CBZ, e) BVO/p-CBZ/NiOOH, the scale bar is 1 μm. BF TEM images of f) BVO, g) BVO/p-CBZ, h) BVO/p-CBZ/NiOOH. i, j) HAADF STEM images of BVO/p-CBZ at different magnifications. k, l) HAADF STEM images of BVO/p-CBZ/NiOOH at different magnifications. m) STEM EDS elemental mapping for BVO/p-CBZ/NiOOH photoanodes.

BVO (JCPDS No. 14-0688),[56] confirming the successful formation of phase-pure BVO. Incorporation of p-CBZ and NiOOH did not alter the BVO crystal structure, consistent with the amorphous nature of the carbazole polymer,[41] and the low thickness of the NiOOH overlayer.[41,51] By contrast, NiOOH deposited directly on FTO exhibits distinct diffraction peaks assigned to crystalline NiOOH (JCPDS No. 27-0956; Figure S7a, Supporting Information). The redox behavior of NiOOH was further confirmed by cyclic voltammetry (Figure S7b, Supporting Information).

The Raman spectrum of pristine BVO (Figure S8, Supporting Information) displays characteristic peaks at 210, 367, and 827 cm^{-1}, consistent with the monoclinic phase of BVO.[42] Similar features are observed for BVO/p-CBZ, BVO/NiOOH, and BVO/p-CBZ/NiOOH, indicating that neither p-CBZ electro-polymerization nor NiOOH electrodeposition alters the Raman-active vibrational modes of BVO.[57] Fourier transform-infrared (FT-IR) spectroscopy was further employed to confirm p-CBZ electro-polymerization on BVO (**Figure 2a**). The CBZ monomer spectrum exhibits a peak at 1329 cm^{-1} (aromatic C–N) and peaks at 1448, 1460, 1480, 1576, and 1590 cm^{-1}, corresponding to aromatic C=C bonds in the benzene ring and carbazole unit.[41,58] Upon electro-polymerization on FTO, slight shifts in peak positions were observed, most notably the C=C stretching vibration, which shifted from 1590 to 1600 cm^{-1}, indicating successful polymerization and strong substrate interaction.[58,59] A similar shift in BVO/p-CBZ confirmed polymer deposition, while the FT-IR spectra of samples prepared with 4, 6, and 8 CV cycles showed progressively increasing peak intensities, consistent with the gradual thickening of the p-CBZ layer (Figure S9, Supporting Information).[60] As shown in Figure S1b, Supporting Information, the photocurrent density decreases with an increase in p-CBZ layer thickness, indicating an optimal layer thickness required for effective charge extraction and improving device performance.

X-ray photoelectron spectroscopy (XPS) was employed to investigate the surface composition and bonding

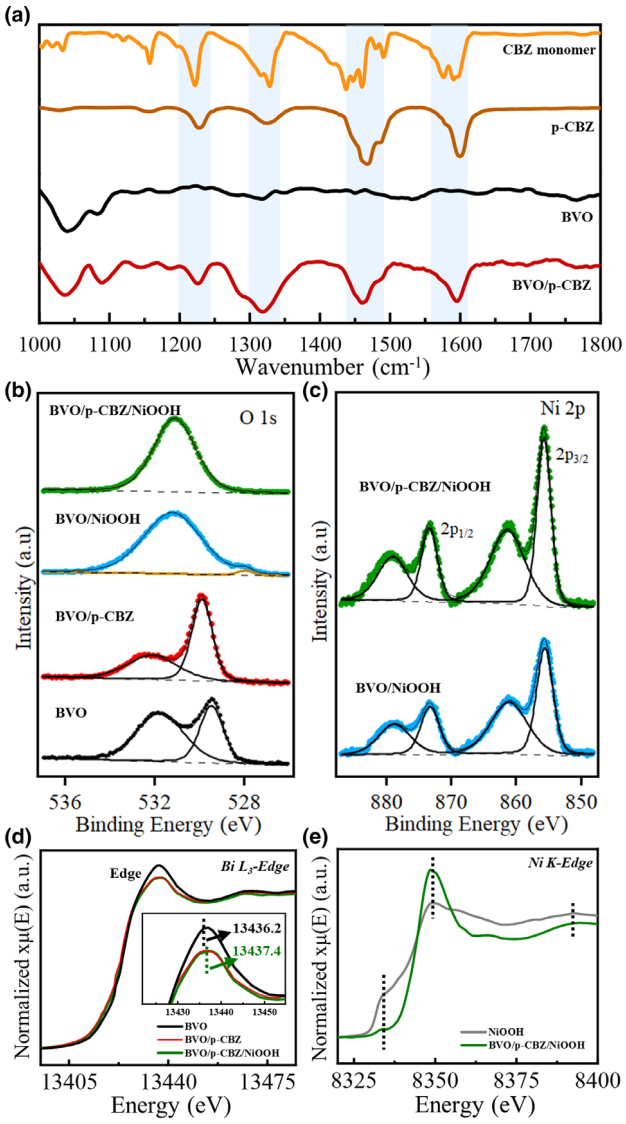

Figure 2. a) FT-IR spectra of the CBZ monomer and p-CBZ over FTO and FTO/BVO samples. XPS spectrum of the b) O 1s and c) Ni 2p regions for the studied photoanodes. XANES spectra of the d) Bi L_3-edge of BVO, BVO/p-CBZ, and BVO/p-CBZ/NiOOH photoanodes and e) Ni *K*-edge of NiOOH powder and BVO/p-CBZ/NiOOH photoanode. The light blue bands on the FT-IR spectra highlight the main peak regions.

environments of the photoanodes (Figure S10, Supporting Information). The O 1s spectrum of pristine BVO (Figure 2b) shows peaks at 529.5 and 531.75 eV, attributed to lattice oxygen and chemisorbed oxygen, respectively.[51] After p-CBZ electro-polymerization, these peaks shift slightly to 529.9 and 532.1 eV, confirming successful polymer incorporation and a new peak emerges at 530.7 eV, assigned to the hydroxyls of water adsorbed on the surface.[61] Upon NiOOH loading, the O 1s spectrum shows a strong peak at ≈531.1 eV, due to the strong overlapping of chemisorbed oxygen peak with NiOOH peak (e.g., –OH from NiOOH or adsorbed water), consistent with surface hydroxyl groups/chemisorbed oxygen species and a new shoulder at 528 eV arises, characteristic of metal oxide species.[57] The BVO/p-CBZ/NiOOH photoanode exhibits a similar profile, with further enhancement of chemisorbed oxygen.

The Ni 2p spectrum (Figure 2c) further verifies NiOOH deposition, showing a Ni $2p_{3/2}$ peak at 855.6 eV for both BVO/NiOOH and BVO/p-CBZ/NiOOH, consistent with NiOOH.[57] The Bi 4f spectra (Figure S11a, Supporting Information) of pristine BVO display peaks at 158.55 and 164.3 eV, corresponding to Bi $4f_{7/2}$ and Bi $4f_{5/2}$ of Bi–O bonds. After p-CBZ deposition, a shift to higher binding energy (≈157.3 eV) indicates strengthened Bi–O interactions, whereas BVO/NiOOH shows a downshift to ≈157.3 eV, suggesting partial reduction of Bi^{3+} to Bi^{2+}. Interestingly, the BVO/p-CBZ/NiOOH heterostructure exhibits an additional Bi $4f_{7/2}$ peak at 159.3 eV, which is consistent with the presence of surface Bi_2O_3.[62] Due to the sequential electro-polymerization of p-CBZ and electrodeposition of NiOOH, the BVO surface is exposed to different oxidative potentials, which promotes the surface oxidation to Bi_2O_3, a transformation previously reported to enhance PEC performance.[63,64]

The V 2p spectra (Figure S11b, Supporting Information) of pristine BVO show V $2p_{3/2}$ and V $2p_{1/2}$ peaks at 516.6 and 524.1 eV, characteristic of V^{5+}.[51] With p-CBZ modification, a slight shift to 516.8 eV reflects local surface interactions with the polymer, while in BVO/-NiOOH, the peak shifts down to 514.9 eV, suggesting partial reduction of V^{5+} to V^{4+} and an increase in oxygen vacancies. Notably, in BVO/p-CBZ/NiOOH the V 2p signal is no longer detected. This attenuation can be attributed to the shadowing effect of the p-CBZ/NiOOH overlayers, combined with electrochemically induced surface reconstruction leading to Bi enrichment and the formation of a thin Bi_2O_3 layer.[65] Such surface oxidation likely arises from the sequential electro-polymerization of p-CBZ followed by NiOOH electrodeposition, during which the BVO surface is exposed to oxidative potentials that promote partial Bi segregation.

To further elucidate the local electronic and structural environments of the photoanodes, X-ray absorption spectroscopy (XAS) was employed on the BVO, BVO/p-CBZ, and BVO/p-CBZ/NiOOH samples. As shown in Figure 2d, the Bi L_3-edge X-ray absorption near-edge structure (XANES) spectrum of BVO exhibits a positive edge shift from 13436.2 to 13437.4 eV after p-CBZ electro-polymerization and subsequent NiOOH electrodeposition.[66] A similar trend is observed at the V K-edge (Figure S11c, Supporting Information), where the edge position slightly shifts from 5504.5 to 5503.3 eV. These subtle variations indicate that the introduction of p-CBZ and NiOOH significantly influences interfacial charge transfer and surface energetics, while the bulk electronic structure of BVO remains essentially unchanged.[41] Moreover, the Ni K-edge spectrum of the BVO/p-CBZ/NiOOH photoanode (Figure 2e) closely matches that of reference NiOOH, confirming the successful deposition of the NiOOH overlayer.[67] It should be noted that the XANES and XPS analyses presented here provide qualitative evidence of relative valence changes, and no absolute quantification of oxygen vacancy concentration is inferred.

The optical properties of the photoanodes are shown in Figure S12, Supporting Information. Pristine BVO (Figure S12a, Supporting Information) exhibits a sharp absorption edge near 500 nm along with a broad absorption band in the 300–500 nm range. Comparable absorbance spectra for BVO/p-CBZ, BVO/NiOOH, and BVO/p-CBZ/NiOOH indicate that neither p-CBZ electro-polymerization nor NiOOH deposition significantly alters the optical response of BVO.[68] This indicates that the enhanced PEC performance originates from the synergistic interfacial effects of p-CBZ and NiOOH rather than from increased light harvesting. Direct band gap values estimated from Tauc

plots (Figure S12b, Supporting Information) were ≈≈2.34 eV for all samples, in good agreement with previous reports.[42]

2.2. Photo-Electrochemical Measurements of BVO Photoanodes

The PEC performance of the synthesized photoanodes was evaluated in a standard three-electrode configuration using 0.5 M potassium borate (KBi) buffer under simulated AM 1.5 G illumination (see Experimental Section for details). As shown in **Figure 3a**, the bare BVO photoanode delivered a modest photocurrent density of 0.9 mA cm^{-2} at 1.23 V versus RHE, limited by severe surface charge recombination. By contrast, BVO/p-CBZ delivered an enhanced photocurrent to 1.9 mA cm^{-2}, representing more than a two-fold increase, confirming the role of p-CBZ as an effective HTL that facilitates charge extraction and suppresses recombination.[41] Further enhancement was obtained upon electrodeposition of NiOOH as an oxygen evolution catalyst. BVO/NiOOH and BVO/p-CBZ/NiOOH exhibited significantly higher photocurrents of 3.8 and 5.6 mA cm^{-2} at 1.23 V versus RHE, representing more than 4- and 6-fold enhancements relative to pristine BVO. While the improvement in BVO/NiOOH is primarily attributed to oxygen vacancies, the superior performance of BVO/p-CBZ/NiOOH arises from the synergistic effects of p-CBZ–mediated charge separation, increased oxygen vacancy concentration, and partial surface transformation to Bi_2O_3.[62] Notably, at a low applied bias of 0.8 V versus RHE, BVO/NiOOH and BVO/p-CBZ/NiOOH still achieved high photocurrents of 3.3 and 4.1 mA cm^{-2}, respectively, demonstrating promise for low-bias PEC operation.[51] Photocurrent trends under chopped and continuous illumination (Figure S12, Supporting Information) were consistent, confirming the stability and reproducibility of the PEC response.

Long-term stability was further examined by chronoamperometry (CA) under continuous illumination. In water oxidation, bare BVO degraded rapidly, undergoing complete decomposition within 9 h (Figure S14, Supporting Information). By contrast, BVO/p-CBZ maintained 40% of its photocurrent after 37 h, indicating improved but still limited stability due to photocorrosion and surface dissolution.[51,69] The BVO/NiOOH photoanode retained only ≈40% of its initial photocurrent after 37 h of operation. The direct BVO/NiOOH interface does not provide sufficiently efficient hole extraction, leading to surface hole accumulation, photocorrosion, and Bi dissolution. Remarkably, the BVO/p-CBZ/NiOOH photoanode sustained a stable photocurrent density of ≈4.3 mA cm^{-2} at 0.8 V versus RHE for 72 h (Figure 3b). Interestingly, an initial increase in photocurrent during the first ≈40 h was observed. This behavior may be related to photo-charging phenomena commonly reported for BVO photoanodes, including light-induced redistribution of defect states and surface restructuring processes that can reduce recombination and improve charge transport. In addition, progressive interfacial modifications, such as NiOOH surface restructuring under operating conditions, may contribute to enhanced oxygen evolution kinetics over time.[32,70] These findings confirm that the NiOOH overlayer not only accelerates oxygen evolution but also plays a pivotal role in mitigating photocorrosion and ensuring durable PEC operation. Post-PEC characterization (XRD, SEM, and HAADF STEM; Figures S15 and S16, Supporting Information) reveals slight surface modification indicating surface reconstruction rather than bulk degradation, further supporting the protective role of NiOOH.

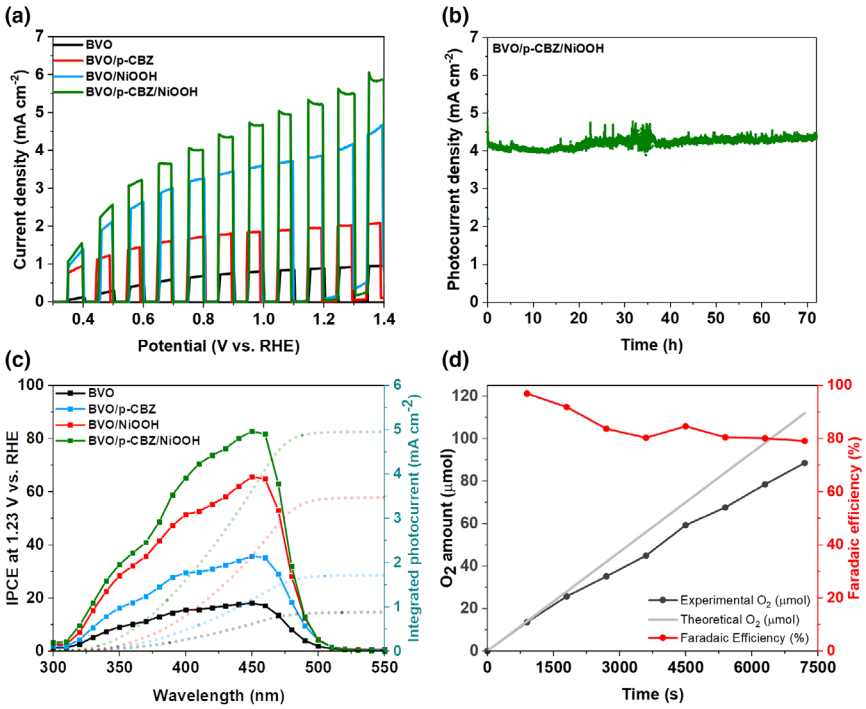

Figure 3. a) Photocurrent density–voltage (LSV) curves of BVO photoanodes with chopped illumination. Voltage scan rate: 10 mV s^{-1}. b) Chronoamperometry test of BVO/p-CBZ/NiOOH at 0.8 V versus RHE. c) IPCE of BVO photoanodes at 1.23 V versus RHE (left) and integrated photocurrent density (right). d) Amount of experimental and theoretical oxygen evolution and calculated Faradaic efficiency at 1.23 V versus RHE. All these measurements were carried out in a 0.5 M potassium borate buffer solution with pH 9.5 under simulated sunlight (Xe source, AM 1.5G filter, 100 mW cm^{-2}).

The charge carrier dynamics of the different photoanodes was further examined using sacrificial hole scavenger experiments (0.1 M Na_2SO_3). Under these conditions, bare BVO displayed a photocurrent of 2.9 mA cm^{-2} at 1.23 V versus RHE, whereas BVO/p-CBZ delivered a 40% higher value of 5.0 mA cm^{-2} (Figure S17a,b, Supporting Information). This enhancement is attributed to the formation of a favorable p–n junction at the BVO/p-CBZ interface, which promotes directional hole transport and reduces recombination.[37,71] The photocurrent onset potential (≈0.3 V vs RHE), measured in the presence of a sacrificial hole scavenger, provides an estimate of the effective flat-band potential of BVO under operating conditions[72,73] and appears slightly more anodic than commonly reported values, suggesting enhanced band bending in the modified photoanode.[74,75] When subjected to long-term stability test, bare BVO suffered ≈35% photocurrent loss after 72 h (Figure S17d, Supporting Information), whereas BVO/p-CBZ retained ≈87% of its initial activity, corresponding to a ≈23% stability

improvement. Post-PEC HAADF STEM characterization (Figure S18, Supporting Information) revealed no significant structural changes, which is attributed to the HTL functionality of p-CBZ, that improves charge separation and suppresses surface recombination (Figure S19, Supporting Information).[17,44]

To gain deeper insight into the origin of the enhanced PEC activity, incident photon-to-current efficiency (IPCE) measurements were carried out (Figure 3c). The pristine BVO photoanode exhibited a maximum IPCE of 18% at 455 nm. Incorporation of p-CBZ and NiOOH led to pronounced improvements, with BVO/p-CBZ/NiOOH reaching a maximum IPCE of 82%, highlighting the synergistic enhancement of charge carrier extraction and transport. Integration of the IPCE spectra with the AM 1.5G photon flux yielded photocurrent densities consistent with those measured under simulated sunlight, validating the accuracy of the measurements. Additional IPCE measurements in the presence of a hole scavenger (Figure S17c, Supporting Information) revealed further increases, reaching 68% and 78% efficiency at 455 nm, for BVO/p-CBZ and BVO/p-CBZ/NiOOH, respectively. These results confirm the role of the p-CBZ layer in facilitating hole transfer and suppressing interfacial recombination, thereby improving spectral response and charge separation efficiency.[76] The applied bias photon-to-current efficiency (ABPE) was calculated (Figure S20, Supporting Information) to evaluate the photon-to-charge conversion efficiency under the application of an external bias. The BVO/p-CBZ/NiOOH photoanode exhibits the highest ABPE, reaching 2.75% at an applied bias of 0.6 V and 1.50% at 0.8 V versus RHE. This enhanced efficiency originates from the substantially increased photocurrent density at lower voltages, reflecting more effective photogenerated charge extraction and utilization. Notably, these ABPE values compare favorably with previously reported BVO photoanodes, as summarized in Table S1, Supporting Information.

The overall water oxidation performance was directly evaluated through oxygen quantification (Figure 3d). The BVO/p-CBZ/NiOOH photoanode generated 88.5 μmol of O_2 at 1.23 V versus RHE, with an average Faradaic efficiency of ≈90%, confirming its excellent catalytic and charge utilization efficiency. Small inaccuracies related to system calibration and gas leaks are believed to account for the remaining 10% FE. Reproducibility is confirmed through repeated FE measurements (Figure S21a, Supporting Information) with error bars, and a 10-hour stability test (Figure S21b, Supporting Information) demonstrates enduring photocurrent and FE. This efficiency, combined with its stable high photocurrent output, places the BVO/p-CBZ/NiOOH system among the most effective BVO-based photoanodes reported to date (Table S1, Supporting Information). Importantly, unlike many BVO systems that exhibit a trade-off between photocurrent density and long-term stability, the hybrid configuration achieves both, underscoring the effectiveness of the dual-modification strategy in enabling efficient and durable solar-driven water oxidation.

2.3. Charge Carrier Dynamics and Interfacial Energetics in BVO Photoanodes

Based on the measurements with the Na_2SO_3 sacrificial hole scavenger, the charge separation efficiency (η_{sep}) and charge injection efficiency (η_{trans}) were extracted (**Figure 4**a,b). These results reveal the beneficial impact of both p-CBZ and NiOOH on charge extraction from BVO, with η_{sep} significantly enhanced up to 1.23 V versus RHE. Moreover, NiOOH dramatically improves η_{trans}, achieving nearly 100% at applied bias as low as 0.8 V versus RHE, confirming its role as an efficient water oxidation co-catalyst.[77] These findings underscore the complementary roles of p-CBZ (charge separation) and NiOOH (charge injection), supported by stronger band bending and enhanced internal electric fields in the BVO/p-CBZ/NiOOH heterostructure.[51,78]

The electronic band structure of the BVO/p-CBZ heterojunction was constructed using literature-reported band positions of BVO[79] and polycarbazole.[50] Direct UPS/XPS measurements were not pursued, as surface-sensitive techniques can be challenging for organic/inorganic interfaces due to vacuum sensitivity and potential modification of the buried interfacial energetics. The resulting band diagram (Figure S22b, Supporting Information) is therefore intended as a schematic representation of the plausible energy-level alignment forming a type-II staggered junction. This configuration enables efficient spatial separation of photogenerated carriers: Holes in BVO are preferentially transferred to the p-CBZ layer, while electrons remain confined within BVO. Such directional carrier flow suppresses interfacial recombination and facilitates charge transport across the heterojunction.[42]

To further probe band energetics, the open-circuit potential (OCP) was measured in the dark (OCP_{dark}) and under AM 1.5G illumination (OCP_{light}). The most positive OCP_{dark} reflects the degree of upward band bending, whereas OCP_{light} corresponds to the flat-band potential (E_f) of the photoanodes.[78] As shown in Figure 4e, BVO/p-CBZ/NiOOH exhibits the most anodic OCP_{dark}, indicating enhanced upward band bending and a stronger built-in potential at the semiconductor/electrolyte interface. By contrast, OCP_{light} remains essentially constant across all samples, suggesting that the bulk electronic structure of BVO is preserved upon surface functionalization. The photovoltage ($\Delta OCP = OCP_{dark} - OCP_{light}$) values confirm this trend: BVO/p-CBZ and BVO/p-CBZ/NiOOH exhibit the highest photovoltages, 0.297 and 0.359 V versus RHE, respectively, consistent with strengthened internal electric fields that improve charge separation and reduce surface recombination.[80]

Further insights into the carrier dynamics were obtained through OCP transient decay measurements (Figure S22a, Supporting Information).[41] Under continuous illumination, band flattening occurs due to quasi-equilibrium of photogenerated carriers. Upon switching to dark conditions, equilibrium is re-established, restoring band bending and triggering recombination governed by charge accumulation in the depletion region.[6] Faster photovoltage decay corresponds to stronger recombination in the dark, which in turn implies more efficient charge extraction under illumination. Indeed, BVO/p-CBZ/NiOOH shows the most rapid decay among all samples (Figure S22a, Supporting Information), highlighting enhanced carrier separation and photocurrent generation during operation.

Carrier lifetimes (τ_n), extracted from OCP decay curves (Figure 4c), were determined as 329 ms for BVO, 235 ms for BVO/p-CBZ, 264 ms for BVO/NiOOH, and 138 ms for BVO/p-CBZ/NiOOH. The shortened lifetime in the ternary system reflects rapid recombination dynamics once illumination is removed, consistent with reduced trap-mediated recombination and accelerated charge transfer under operating conditions.[6,41] Collectively, these findings underscore the synergistic effects of p-CBZ and NiOOH: The polymer interlayer promotes effective hole extraction and suppresses recombination, while NiOOH enhances interfacial charge transfer, together enabling superior PEC water oxidation performance.

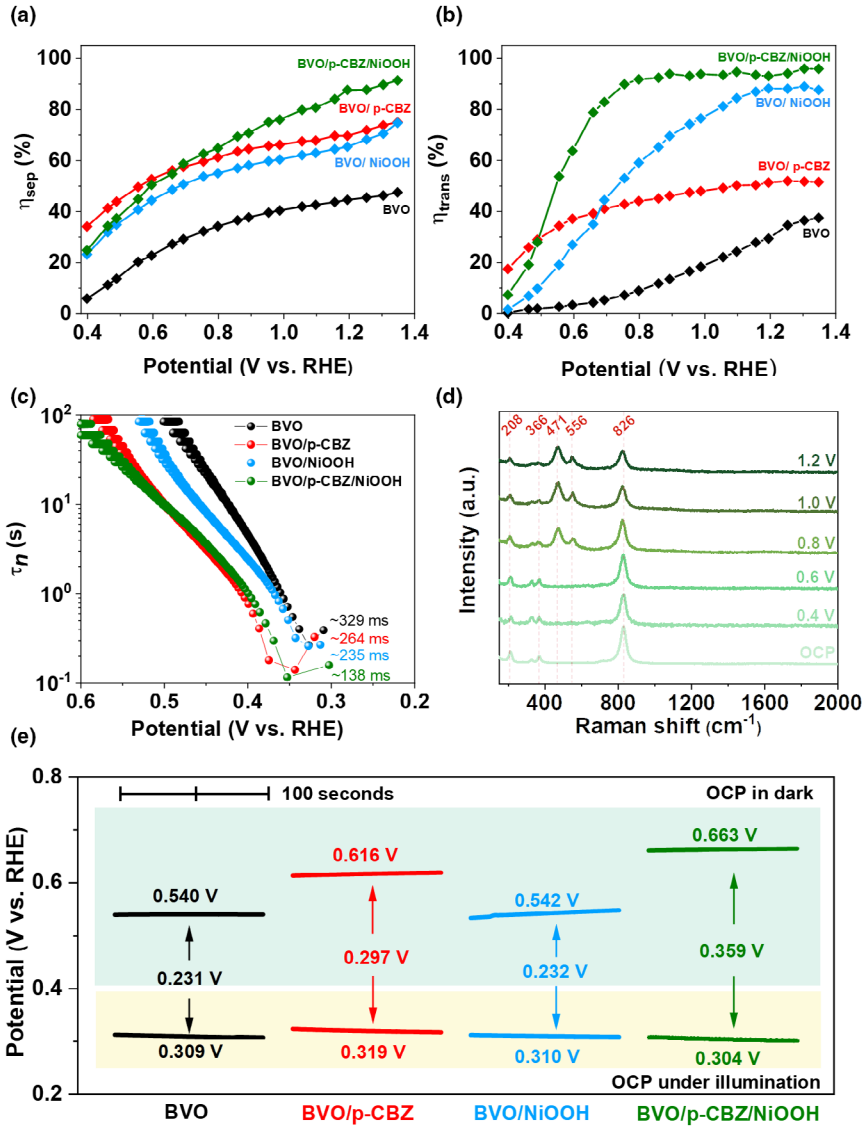

Figure 4. a) Charge separation (η_{sep}). b) Charge transfer (η_{trans}), efficiencies of BVO photoanodes. c) OCP-derived carrier lifetimes. d) In situ Raman spectra of BVO/p-CBZ/NiOOH under different applied potentials versus RHE and e) OCP plots in the dark and under illumination. All these measurements were carried out in a 0.5 M potassium borate buffer solution with pH 9.5 under simulated sunlight (Xe lamp, AM 1.5G filter, 100 mW cm^{-2}).

In situ Raman spectroscopy (Figure 4d) was employed to monitor the structural evolution of the BVO/p-CBZ/NiOOH heterostructure under anodic bias in borate buffer. At potentials below 0.6 V versus RHE, the spectra are dominated by the characteristic vibrational modes of monoclinic BVO. Upon increasing the potential to 0.8 V versus RHE (near the OER onset), two distinct bands emerge at 471 and 556 cm^{-1}, corresponding to the E_g bending and A_{1g} stretching modes of γ-NiOOH, respectively. The progressive growth of these γ-NiOOH features with increasing anodic bias indicates a potential-driven reconstruction of the Ni species toward higher-valence oxyhydroxide states under operational conditions. This operando structural evolution supports the proposed mechanism in which activation of the NiOOH cocatalyst contributes to the enhanced water oxidation performance.[24]

2.4. Insights into Charge Carrier Dynamics through Impedance and IMPS/IMVS Analysis

Further insights into charge carrier dynamics were obtained from electrochemical impedance spectroscopy (EIS), intensity-modulated photocurrent spectroscopy (IMPS), and intensity-modulated photovoltage spectroscopy (IMVS). The Nyquist plots from EIS (Figure S23a, Supporting Information) displayed a single semicircle, well described by a simple Randles circuit. The semicircle diameter, which reflects charge transport and transfer kinetics, scaled inversely with PEC activity. Pristine BVO exhibited the largest semicircle, consistent with its poor electrical conductivity and sluggish water oxidation kinetics. By contrast, BVO/p-CBZ showed a substantially smaller semicircle, reflecting improved hole extraction and suppressed recombination at the p–n junction interface.[43] Both BVO/NiOOH and BVO/p-CBZ/NiOOH electrodes exhibited further reduced semicircles, attributable to accelerated interfacial charge transfer enabled by NiOOH catalysis.[51] The series resistance (R_s), which is the combined resistance of the electrolyte, contacts, and the underlying FTO substrate, remained essentially constant for all samples (≈40 Ω cm^{-2}), since it was controlled by the sheet resistance of the FTO substrate (Figure S23b, Tables S2–S4, Supporting Information).

The extracted charge transfer resistance (R_{ct}) and capacitance (C), corresponding to the resistance of interfacial charge transfer at the photoanode/electrolyte interface and the non-ideal capacitive behavior of the electrode surface, are summarized in **Figure 5**a,b and Tables S2–S4, Supporting Information. BVO and BVO/p-CBZ showed similar R_{ct} trends with applied bias, indicating comparable intrinsic catalytic activity, though the consistently lower resistance of BVO/p-CBZ confirmed improved charge transport through more effective charge separation. Incorporating NiOOH caused a pronounced drop in R_{ct}, especially below 0.8 V versus RHE, where band bending is insufficient to fully suppress charge recombination. This behavior underscores the catalytic function of NiOOH in accelerating water oxidation. Notably, the BVO/p-CBZ/NiOOH photoanode displayed the lowest R_{ct} across the full potential range, highlighting the complementary roles of p-CBZ (hole extraction, recombination suppression) and NiOOH (catalytic charge transfer) in establishing highly efficient charge carrier dynamics.

Capacitance trends further corroborated these effects (Figure 5b). Higher capacitance correlated with reduced R_{ct}, suggesting that the charge storage mechanisms are mainly controlled by the NiOOH catalyst. For Ni-based catalysts, capacitance has been proposed as a descriptor of catalytic activity,[81] in good agreement with the present results.

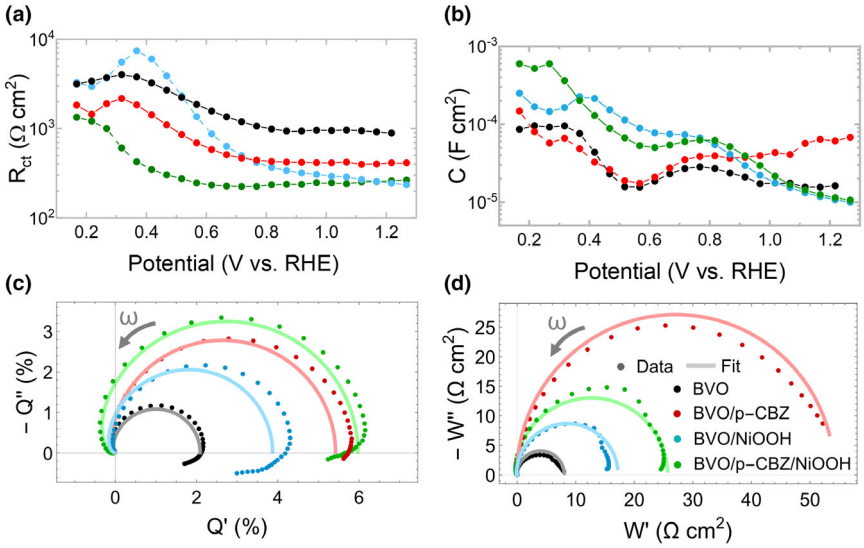

Figure 5. a) Charge transfer resistance (R_{ct}) and b) capacitance (C) as function of the applied potential extracted from EIS. c) Intensity-Modulated Photocurrent Spectroscopy (IMPS) and d) Intensity-Modulated Photovoltage Spectroscopy (IMVS). Experimental (dots) and fitted (lines) spectra for the four investigated devices: BVO (black), BVO/p-CBZ (red), BVO/NiOOH (blue), and BVO/p-CBZ/NiOOH (green).

A well-defined peak around 0.8 V versus RHE corresponds to the V^{4+}/V^{5+} redox couple of BVO and the associated formation of oxygen vacancies.[82] This in situ technique provides mechanistically relevant insight into vacancy-related electronic states under operating conditions, whereas ex situ approaches such as XPS and EPR may be limited by the instability of these defect states outside the electrochemical environment.

Complementary IMPS and IMVS measurements provided additional kinetic insights (Figure 5c,d and Figure S24, Supporting Information). At low frequency, the IMPS response reflects the differential external quantum efficiency (EQE_{diff}).[83] The addition of p-CBZ markedly enhanced EQE_{diff} relative to bare BVO, with further improvements observed upon NiOOH incorporation. IMVS (W) measurements, which are related to IS (Z) and IMPS (Q) via $W = Z \times Q$, supported this trend, representing the photovoltage generated per incident photon.[84,85]

To quantify these effects, we simultaneously fitted the EIS, IMPS, and IMVS data for all electrodes following the procedure developed in our previous work,[7] and summarized in the experimental method of the Supporting Information, with the resulting parameters summarized in Table S3a, Supporting Information (full data set in Table S3b, Supporting Information). Bare BVO exhibited a low EQE_{diff} of 2.1%. Modification with either NiOOH or p-CBZ increased EQE_{diff} by approximately two- and 2.5-fold, respectively, while the combined BVO/p-CBZ/NiOOH system reached 6.0%. These trends can be rationalized by the relation:

$$EQE_{Diff} = \eta_{opt} .a.\eta_{sep}.\eta_{col}, \quad (1)$$

where η_{opt}, a, η_{sep}, and η_{col} denotes the optical efficiency, absorbance, charge separation efficiency, and charge collection efficiency. In this work, η_{opt} and a are assumed to be constant across devices. From Table S3, Supporting Information, we can note that the improvements of the EQE_{Diff} stem mainly from the improvements of charge separation efficiency (η_{sep}), which increases in the order: BVO < BVO/NiOOH < BVO/p-CBZ < BVO/p-CBZ/NiOOH.

Collection efficiency (η_{col}) scales similarly to EQE_{diff}. Notably, p-CBZ mainly reduces bulk recombination, as reflected by an increase in τ_{rec}, while the diffusion coefficient (D) exhibits only minor changes compared with bare BVO (Table S3, Supporting Information). As a result, the effective diffusion length ($L = \sqrt{D\tau_{rec}}$) increases significantly. The extracted L values exceed the film thickness (≈500 nm), indicating that photogenerated carriers can be efficiently collected across the electrode. It is important to emphasize that this effective diffusion length describes macroscopic transport within the nanostructured electrode under operando conditions and should be distinguished from the intrinsic microscopic diffusion length of compact BVO (≈70 nm). Altogether, the combined EIS, IMPS, and IMVS analyses reveal that p-CBZ primarily promotes charge separation and transport, whereas NiOOH accelerates interfacial catalytic charge transfer, resulting in a synergistic enhancement of the photoelectrochemical efficiency.

2.5. Mechanistic Insights into Synergistic Charge Regulation in BVO Photoanodes

Based on OCP, EIS, and IMPS/IMVS measurements, the following mechanism (**Figure 6**) is proposed:

Under illumination, BVO absorbs photons and generates electron–hole pairs. In the case of bare BVO, most of these carriers recombine before contributing to photocurrent, leading to poor PEC activity. Upon polycarbazole addition, a p–n junction was formed between BVO and p-CBZ, acting as a HTL and a passivating interlayer. It reduces surface recombination by passivating trap states on BVO and simultaneously serves as a conductive pathway for photogenerated holes. This increases band bending and strengthens the internal electric field at the BVO surface, thereby improving charge separation (η_{sep}) and charge collection (η_{col}), together increasing the EQE_{diff} and suppressing the surface recombination losses. Electrodeposited NiOOH serves as a highly active co-catalyst for the oxygen evolution reaction (OER). Its hydroxyl-rich structure provides abundant adsorption sites for OER intermediates and increases the OER kinetics through Ni valence-state reconstruction ($Ni^{2+}/Ni^{3+}/Ni^{4+}$) and catalytic activation during OER. In parallel, NiOOH efficiently extracts photogenerated holes from the BVO/p-CBZ interface, thereby reducing interfacial charge transfer resistance and lowering the overpotential required for water oxidation. Additionally, the combined surface treatments (p-CBZ polymerization followed by NiOOH deposition) induced a partial oxidation of the BVO surface to Bi_2O_3 and increased the concentration of oxygen vacancies, while leaving the bulk composition unchanged. Evidence from XPS, XANES, and EIS confirms these modifications, which collectively enhance charge injection into the electrolyte and contribute to the improved photoelectrochemical performance.

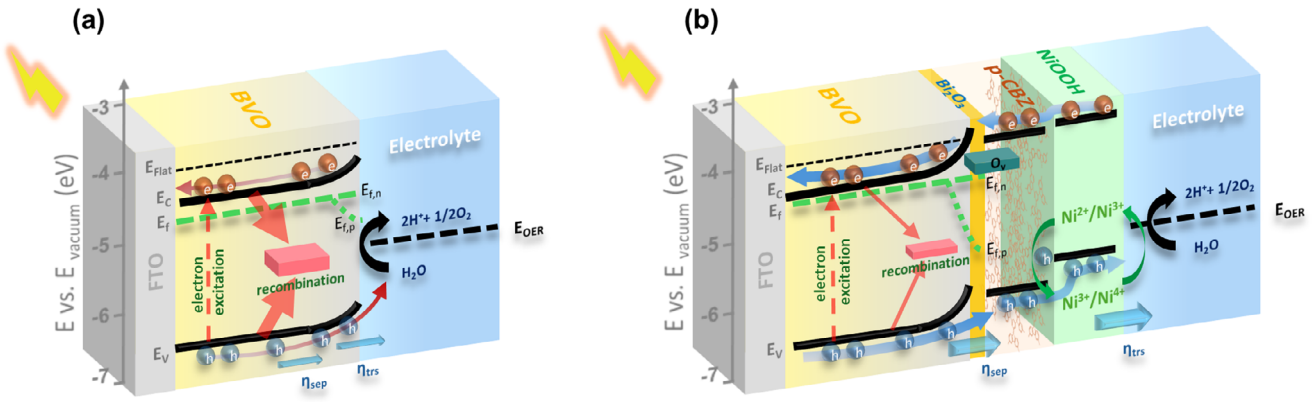

Figure 6. Schematic model showing the proposed PEC operation mechanisms in a) BVO, b) BVO/p-CBZ/NiOOH photoanodes under illumination. E_{Flat}: Flat-band potential; E_f: Fermi level, E_c: Conduction band; E_v: Valence band; *e*: Electron; h^+: Hole; $E_{f,n}$: Quasi-Fermi level for electrons; $E_{f,p}$: Quasi-Fermi level for holes. η_{sep}: Charge separation efficiency; η_{trans}: Charge injection efficiency; O_v: Oxygen vacancies. E_{OER}: Oxygen Evolution Reaction potential.

The p-CBZ layer functions as a charge separation engine by doubling EQE_{diff} and enhancing internal electric fields via Type-II band alignment, while NiOOH acts as a catalytic valve that maximizes η_{trans} to ≈100% and minimizes R_{ct}. Their synergy is evidenced by a low carrier lifetime (138 ms) and R_{ct}, where rapid p-CBZ-mediated hole extraction is coupled with immediate NiOOH-catalyzed consumption to eliminate interfacial recombination. Thus, the integration of p-CBZ and NiOOH yields a cooperative effect: p-CBZ enhances charge separation and transport, while NiOOH accelerates surface charge transfer and catalysis. This synergy minimizes both bulk and interfacial recombination, maximizes photocurrent density, and suppresses photocorrosion by passivating surface defects. As a result, the BVO/p-CBZ/NiOOH photoanode demonstrates superior PEC efficiency and long-term operational stability compared with pristine BVO.

3. Conclusions

We have successfully electro-polymerized carbazole (p-CBZ), a well-established hole transport material, onto BVO photoanodes under optimized conditions. The p-CBZ layer passivates surface recombination and enhances charge separation, as confirmed by electrochemical and optoelectronic analyses. Subsequent electrodeposition of NiOOH, a highly active OER catalyst, further accelerates interfacial charge transfer, enabling efficient hole injection into the electrolyte. The resulting BVO/p-CBZ/NiOOH photoanode delivers a photocurrent density of 5.6 mA cm^{-2} at 1.23 V versus RHE with remarkable stability over 72 h, owing to the synergistic effects of improved charge separation, suppressed recombination, and enhanced surface catalysis. This optimized architecture establishes a rational design strategy for BVO-based photoanodes and highlights the potential of integrating functional interlayers to achieve both high-performance and long-term durability in practical PEC water splitting.

4. Experimental Section

Detailed information related to the synthesis of active electrodes, physicochemical characterization, and electrochemical evaluation of bifunctional electrodes towards UOR and supercapacitor application is provided in Supporting Information.

Acknowledgements

The authors thank support from the projects PID2023-152771OB-I00 and PID2023-149158OB-C43 and RED2022-134508-T (CAT&SCALE), funded by MICIU/AEI/10.13039/501100011033/ and by "ERDF A way of making Europe." We are also grateful to the Serveis Centrals d'Instrumentació Científica from the Universitat Jaume I (SCIC-UJI) for providing all the characterization facilities. J.E.D. is grateful to Consejo Nacional de Investigaciones Científicas y Técnicas (CONICET) of Argentina for the financial support. We also thank Diamond light source for providing beamtime with experiments reference 39050 and MG40113-1, and Dr. Miguel Gómez-González for all the technical support with these measurements. ICN2 is funded by the CERCA Program/Generalitat de Catalunya. This study is part of the Advanced Materials programme and was supported by MCIN with funding from European Union NextGenerationEU (PRTR-C17.I1) and by Generalitat de Catalunya (In-CAEM Project). ICN2 is supported by the Severo Ochoa program from Spanish MCIN/AEI (Grant No.: CEX2021-001214-S). Authors acknowledge the use of instrumentation as well as the technical advice provided by the Joint Electron Microscopy Center at ALBA (JEMCA). ICN2 acknowledges funding from Grant IU16-014206 (METCAM-FIB) funded by the European Union through the European Regional Development Fund (ERDF), with the support of the Ministry of Research and Universities, Generalitat de Catalunya. ICN2 is founding member of e-DREAM.[86]

Conflict of Interest

The authors declare no conflict of interest.

Supporting Information

Supporting Information is available from the Wiley Online Library or from the author.

Keywords

bismuth vanadate, photoanode, polycarbazole, solar fuels, water splitting

Received: December 31, 2025
Revised: February 21, 2026
Published online: February 24, 2026

[1] Y. Chen, X. Li, H. Yang, Y. Huang, *Small* **2024**, *20*, 2307255.
[2] H. Kong, H. Yang, J. S. Park, W. S. Chae, H. Y. Kim, J. Park, J. H. Lee, S. Y. Choi, M. Park, H. Kim, Y. Song, H. Park, J. Yeo, *Adv. Funct. Mater.* **2022**, *32*, 2200403.
[3] S. Zhao, B. Liu, K. Li, S. Wang, G. Zhang, Z. J. Zhao, T. Wang, J. Gong, *Nat. Commun.* **2024**, *15*, 2452.
[4] P.-W. Chen, K. Li, Y.-X. Yu, W.-D. Zhang, *Appl. Surf. Sci.* **2017**, *392*, 608.
[5] A. Kasa, L. S. Arumugam, A. Vanleenhove, V. Jose, T. Conard, D. Santos, J. D'Haen, A. Simbula, L. Lutsen, J. E. Durantini, S. Giménez, G. Brammertz, S. Shukla, B. Vermang, *Nano Lett.* **2025**, *25*, 1234.
[6] H. Zhang, D. Li, W. J. Byun, X. Wang, T. J. Shin, H. Y. Jeong, H. Han, C. Li, J. S. Lee, *Nat. Commun.* **2020**, *11*, 4622.
[7] R. Arcas, D. Cardenas-Morcoso, M. C. Spadaro, M. García-Tecedor, C. A. Mesa, J. Arbiol, F. Fabregat-Santiago, S. Giménez, E. Mas-Marzá, *Sol. RRL* **2022**, *6*, 2200345.
[8] M. Wang, Z. Wang, B. Zhang, W. Jiang, X. Bao, H. Cheng, Z. Zheng, P. Wang, Y. Liu, M. H. Whangbo, Y. Li, Y. Dai, B. Huang, *ACS Catal.* **2020**, *10*, 13031.
[9] T. Li, J. He, B. Peña, C. P. Berlinguette, *Angew. Chem.* **2016**, *128*, 1801.
[10] P. Arunachalam, M. S. Amer, A. M. Al-Mayouf, A. A. Alsaleh, *ChemCatChem* **2024**, *16*, e202301344.
[11] W. Zhu, Y. Yuan, Y. Ma, *SustainableEnergy Fuels* **2024**, *8*, 1077.
[12] H. S. Park, K. E. Kweon, H. Ye, E. Paek, G. S. Hwang, A. J. Bard, *J. Phys. Chem. C* **2011**, *115*, 17870.
[13] C. Tao, Y. Jiang, Y. Ding, B. Jia, R. Liu, P. Li, W. Yang, L. Xia, L. Sun, B. Zhang, *JACS Au* **2023**, *3*, 1851.
[14] D. He, Q. Wang, W. Zhang, X. Liu, X. Cui, *ChemPhotoChem.* **2023**, *7*, e202300080.
[15] S. Ju, N. Lee, H. Sung, S. Son, N. Kim, J. Kim, J. k. Kim, H. Lee, *J. Mater. Chem. A* **2023**, *11*, 17644.
[16] C. W. Moon, M. J. Choi, J. K. Hyun, H. W. Jang, *Nanoscale Adv.* **2021**, *3*, 5981.
[17] B. J. Trześniewski, W. A. Smith, *J. Mater. Chem. A* **2016**, *4*, 2919.
[18] S. Yu, C. Su, Z. Xiao, Y. Kuang, X. Gong, X. He, J. Liu, Q. Jin, Z. Sun, *RSC Adv.* **2025**, *15*, 815.
[19] S. Ren, M. Sun, X. Guo, X. Liu, X. Zhang, L. Wang, *ACS Catal.* **2022**, *12*, 1686.
[20] Y. Li, Q. Wang, X. Hu, Y. Meng, H. She, L. Wang, J. Huang, G. Zhu, *Chem. Eng. J.* **2022**, *433*, 133592.
[21] R. Gao, D. He, L. Wu, K. Hu, X. Liu, Y. Su, L. Wang, *Angew. Chem.* **2020**, *132*, 6272.
[22] T. Palaniselvam, L. Shi, G. Mettela, D. H. Anjum, R. Li, K. P. Katuri, P. E. Saikaly, P. Wang, *Adv. Mater. Interfaces* **2017**, *4*, 1700540.
[23] H. Chen, J. Li, L. Meng, S. Bae, R. Erni, D. F. Abbott, S. Li, C. A. Triana, V. Mougel, G. R. Patzke, *Adv. Funct. Mater.* **2023**, *33*, 2214470.
[24] J. B. Pan, B. H. Wang, J. B. Wang, H. Z. Ding, W. Zhou, X. Liu, J. R. Zhang, S. Shen, J. K. Guo, L. Chen, C. T. Au, L. L. Jiang, S. F. Yin, *Angew. Chem. Int. Ed.* **2021**, *60*, 1433.
[25] Y. Liu, Z. Zhang, K. Wang, X. Tan, J. Chen, X. Ren, F. Jiang, *Adv. Energy Mater.* **2024**, *14*, 2400561.
[26] Y. Wang, Y. Chen, Y. Yun, X. Hong, Y. Huang, H. Ji, *Appl. Catal. B Environ. Energy* **2024**, *358*, 124375.
[27] Y. Chen, J. Huang, J. Zhou, X. Li, H. Yang, Y. Huang, *Mater. Today Adv.* **2025**, *25*, 100554.
[28] H. Ali, M. Liu, S. Ali, A. Ali, P. M. Ismail, R. Ullah, S. Ali, F. Raziq, M. Bououdina, S. Hayat, U. Ali, Y. Zhou, X. Wu, L. Zhong, L. Zhu, H. Xiao, P. Xia, L. Qiao, *J. Colloid Interface Sci.* **2024**, *665*, 500.
[29] A. Guo, X. Wu, S. H. Ali, H. Shen, L. Chen, Y. Li, B. Wang, *RSC Adv.* **2024**, *14*, 9609.
[30] L. S. Arumugam, J. E. Durantini, J. Follana-Berná, F. Schiller, A. Etxebarria, L. Forzanini, S. Barja, Á. Sastre-Santos, S. Giménez, *ACS Appl. Energy Mater.* **2025**, *8*, 5056.
[31] L. Zhu, X. Tian, G. Shi, W. Zhang, P. Tang, M. Bououdina, S. Ali, P. Xia, *Chin. Chem. Lett.* **2025**, *36*, 111088.
[32] S. Bae, T. Moehl, E. Service, M. Kim, P. Adams, Z. Wang, Y. Choi, J. Ryu, S. D. Tilley, *Nat. Commun.* **2024**, *15*, 9439.
[33] W. T. Hong, M. Han, Y. Li, J. Kim, J. Lee, W. Yang, T. Yu, J. K. Kim, *ACS Mater. Lett.* **2024**, *6*, 4168.
[34] Y. X. Ma, B. Gao, J. He, J. F. Ma, Y. Zhao, *Chem. Eng. J.* **2021**, *422*, 130096.
[35] L. Wang, J. Zhang, Y. Li, Y. Shi, J. Huang, Q. Mei, L. Wang, F. Ding, B. Bai, Q. Wang, *Appl. Catal. B* **2023**, *336*, 122934.
[36] S. Li, M. Li, F. Chen, H. Huang, *J. Mater. Chem. A* **2022**, *10*, 16646.
[37] Y. Zhang, H. Lv, Z. Zhang, L. Wang, X. Wu, H. Xu, *Adv. Mater.* **2021**, *33*, 2005882.
[38] T. Soltani, A. Tayyebi, B. K. Lee, *Sol. Energy Mater. Sol. Cells* **2018**, *185*, 325.
[39] P. Mane, H. Bae, V. Burungale, S. W. Lee, M. Misra, H. Parbat, A. N. Kadam, J. S. Ha, *Chemosphere* **2022**, *308*, 136323.
[40] H. Pei, S. Xu, Y. Zhang, Y. Zhou, R. Li, T. Peng, *Appl. Catal. B* **2022**, *318*, 121857.
[41] J. W. Yang, S. G. Ji, C. S. Jeong, J. Kim, H. R. Kwon, T. H. Lee, S. A. Lee, W. S. Cheon, S. Lee, H. Lee, M. S. Kwon, J. Moon, J. Y. Kim, H. W. Jang, *Energy Environ. Sci.* **2024**, *17*, 2541.
[42] K. Tian, Z. Xu, H. Yang, G. Chen, P. An, J. Zhang, S. Liu, J. Yan, *Adv. Energy Mater.* **2024**, *14*, 2304195.
[43] J. Wang, N. Muhammad, Z. Chuai, W. Xu, X. Tan, Q. Zhou, Y. Yu, J. Guo, T. Li, B. Xu, *Angew. Chem. Int. Ed.* **2025**, *64*, e202418522.
[44] K. Radhakrishna, S. B. Manjunath, D. Devadiga, R. Chetri, A. T. Nagaraja, *ACS Omega* **2023**, *8*, 3635.
[45] I. Burgués-Ceballos, F. Hermerschmidt, A. V. Akkuratov, D. K. Susarova, P. A. Troshin, S. A. Choulis, *ChemSusChem* **2015**, *8*, 4209.
[46] Y. Xie, X. Wang, Q. Chen, S. Liu, Y. Yun, Y. Liu, C. Chen, J. Wang, Y. Cao, F. Wang, T. Qin, W. Huang, *Macromolecules* **2019**, *52*, 4757.
[47] M. Ramezanitaghartapeh, A. F. Hollenkamp, M. Musameh, P. J. Mahon, *Electrochim. Acta* **2021**, *391*, 138865.
[48] G. Bagdžiūnas, D. Palinauskas, *Biosensors* **2020**, *10*, 178.
[49] A. Srivastava, P. Chakrabarti, *Superlattice. Microst.* **2015**, *88*, 723.
[50] L. Wang, W. Lian, B. Liu, H. Lv, Y. Zhang, X. Wu, T. Wang, J. Gong, T. Chen, H. Xu, *Adv. Mater.* **2022**, *34*, 2108217.
[51] J. Cui, M. Daboczi, M. Regue, Y. C. Chin, K. Pagano, J. Zhang, M. A. Isaacs, G. Kerherve, A. Mornto, J. West, S. Gimenez, J. S. Kim, S. Eslava, *Adv. Funct. Mater.* **2022**, *32*, 2205556.
[52] A. Et Taouil, E. Contal, S. Lakard, B. Lakard, *J. Electroanal. Chem.* **2021**, *894*, 115367.
[53] R. Rubio, M. B. Suarez, M. E. Pérez, D. A. Heredia, G. M. Morales, E. N. Durantini, L. Otero, M. Gervaldo, J. E. Durantini, *Electrochim. Acta* **2023**, *458*, 142552.
[54] M. Thangamuthu, Q. Ruan, P. O. Ohemeng, B. Luo, D. Jing, R. Godin, J. Tang, *Chem. Rev.* **2022**, *122*, 11778.
[55] Y. Tang, C. Wang, Y. Guo, L. Mao, X. Cai, Y. Li, B. Liu, X. Tan, J. Ye, T. Yu, *Chin. Chem. Lett.* **2025**, *36*, 112275.
[56] J. Huang, Z. Yang, X. Yuan, L. Wang, H. She, Q. Wang, *Chin. Chem. Lett.* **2025**, *36*, 111062.
[57] H. Luo, C. Liu, Y. Xu, C. Zhang, W. Wang, Z. Chen, *Int. J. Hydrog. Energy* **2019**, *44*, 30160.
[58] V. Raj, D. Madheswari, M. M. Ali, *J. Appl. Polym. Sci.* **2010**, *116*, 147.
[59] E. Marimuthu, V. Murugesan, *SN Appl. Sci.* **2019**, *1*, 446.
[60] Y. H. Chiu, C. Kongvarhodom, M. Saukani, S. Yougbaré, H. M. Chen, Y. F. Wu, L. Y. Lin, *Int. J. Hydrog. Energy* **2024**, *89*, 142.
[61] H. Idriss, *Surf. Sci.* **2021**, *712*, 121894.
[62] P. Chakthranont, L. C. Seitz, T. F. Jaramillo, *J. Phys. Chem. Lett.* **2015**, *6*, 3702.
[63] B. Khan, M. B. Faheem, K. Peramaiah, J. Nie, H. Huang, Z. Li, C. Liu, K.-W. Huang, J.-H. He, *Nat. Commun.* **2024**, *15*, 6990.
[64] F. M. Toma, J. K. Cooper, V. Kunzelmann, M. T. McDowell, J. Yu, D. M. Larson, N. J. Borys, C. Abelyan, J. W. Beeman, K. M. Yu, J. Yang, L. Chen, M. R. Shaner, J. Spurgeon, F. A. Houle, K. A. Persson, I. D. Sharp, *Nat. Commun.* **2016**, *7*, 12012.

[65] A. S. Racz, M. Menyhard, *Appl. Surf. Sci. Adv.* **2025**, *30*, 100872.
[66] L. Wang, Y. Wu, S. Mao, J. Zhou, Y. Zhang, X. Zheng, X. Wu, H. Xu, *Adv. Mater.* **2025**, *37*, 2412345.
[67] A. S. M. Ismail, I. Garcia-Torregrosa, J. C. Vollenbroek, L. Folkertsma, J. G. Bomer, T. Haarman, M. Ghiasi, M. Schellhorn, M. Nachtegaal, M. Odijk, A. van den Berg, B. M. Weckhuysen, F. M. F. de Groot, *ACS Catal.* **2021**, *11*, 12324.
[68] J. Miao, C. Lin, X. Yuan, Y. An, Y. Yang, Z. Li, K. Zhang, *Nat. Commun.* **2024**, *15*, 1234.
[69] S. Zhang, I. Ahmet, S.-H. Kim, O. Kasian, A. M. Mingers, P. Schnell, M. Kölbach, J. Lim, A. Fischer, K. J. J. Mayrhofer, S. Cherevko, B. Gault, R. van de Krol, C. Scheu, *ACS Appl. Energy Mater.* **2020**, *3*, 9523.
[70] M. Huang, Z. Huang, H. Zhu, *Nano Energy* **2020**, *70*, 104525.
[71] M. Xie, J. Bian, M. Humayun, Y. Qu, Y. Feng, L. Jing, *Chem. Commun.* **2015**, *51*, 2821.
[72] D. Cardenas-Morcoso, R. Ifraemov, M. García-Tecedor, I. Liberman, S. Gimenez, I. Hod, *J. Mater. Chem. A* **2019**, *7*, 11143.
[73] A. Hankin, F. E. Bedoya-Lora, J. C. Alexander, A. Regoutz, G. H. Kelsall, *J. Mater. Chem. A* **2019**, *7*, 26162.
[74] M. N. Shaddad, M. A. Ghanem, A. M. Al-Mayouf, S. Gimenez, J. Bisquert, I. Herraiz-Cardona, *ChemSusChem* **2016**, *9*, 2779.
[75] B. J. Trześniewski, I. A. Digdaya, T. Nagaki, S. Ravishankar, I. Herraiz-Cardona, D. A. Vermaas, A. Longo, S. Gimenez, W. A. Smith, *Energy Environ. Sci.* **2017**, *10*, 1517.
[76] C. Nomellini, A. Polo, C. A. Mesa, E. Pastor, G. Marra, I. Grigioni, M. V. Dozzi, S. Giménez, E. Selli, *ACS Appl. Mater. Interfaces* **2023**, *15*, 34567.
[77] X. Yang, J. Cui, L. Lin, A. Bian, J. Dai, W. Du, S. Guo, J. Hu, X. Xu, *Adv. Sci.* **2024**, *11*, 2305678.
[78] M. Zhong, T. Hisatomi, Y. Kuang, J. Zhao, M. Liu, A. Iwase, Q. Jia, H. Nishiyama, T. Minegishi, M. Nakabayashi, N. Shibata, R. Niishiro, C. Katayama, H. Shibano, M. Katayama, A. Kudo, T. Yamada, K. Domen, *J. Am. Chem. Soc.* **2015**, *137*, 5053.
[79] H. Ullah, A. A. Tahir, T. K. Mallick, *Appl. Catal. B* **2018**, *224*, 895.
[80] L. Ding, L. Wang, S. Chu, W. Zhai, J. Li, X. Li, Z. Jiao, *ACS Appl. Energy Mater.* **2024**, *7*, 2963.
[81] D. Kutyła, M. Fukumoto, H. Takahashi, M. Wojnicki, P. Żabiński, *Meta* **2024**, *14*, 904.
[82] F. S. Hegner, I. Herraiz-Cardona, D. Cardenas-Morcoso, N. López, J.-R. Galán-Mascarós, S. Gimenez, *ACS Appl. Mater. Interfaces* **2017**, *9*, 37671.
[83] S. Ravishankar, C. Aranda, P. P. Boix, J. A. Anta, J. Bisquert, G. Garcia-Belmonte, *J. Phys. Chem. Lett.* **2018**, *9*, 3099.
[84] A. O. Alvarez, S. Ravishankar, F. Fabregat-Santiago, *Small Methods* **2021**, *5*, 2000854.
[85] L. Bertoluzzi, J. Bisquert, *J. Phys. Chem. Lett.* **2017**, *8*, 172.
[86] R. Ciancio, R. E. Dunin-Borkowski, E. Snoeck, M. Kociak, R. Holmestad, J. Verbeeck, A. I. Kirkland, G. Kothleitner, J. Arbiol, *Microsc. Microanal.* **2022**, *28*, 2900.